CFD modelling and simulation of drill cuttings transport efficiency in annular bends: Effect of particle size polydispersity

CFD Modelling and Simulation of Drill Cuttings Transport Efficiency in Annular Bends: Effect of Particle Size Polydispersity

[a,b]Emmanuel I. Epelle, [a]Winifred Obande, [d]Jude A. Okolie, [c]Tabbi Wilberforce, [a]Dimitrios I. Gerogiorgis*

[a]*Institute for Materials and Processes (IMP), School of Engineering, University of Edinburgh, The King's Buildings, Edinburgh, EH9 3FB, United Kingdom*

[b]*School of Computing, Engineering & Physical Sciences, University of the West of Scotland, Paisley PA1 2BE, United Kingdom*

[c]*Mechanical Engineering and Design, Aston University, School of Engineering and Applied Science, Aston Triangle, Birmingham, B4 7ET, United Kingdom*

[d]*Department of Chemical and Biological Engineering, University of Saskatchewan, Saskatoon, Canada*

*Corresponding author: d.gerogiorgis@ed.ac.uk

Abstract

This study analyses the impact of particle polydispersity using the Eulerian-Eulerian (EE) and Lagrangian-Eulerian (LE) modelling approaches in the context of wellbore cleaning operations in the drilling industry. Spherical particles of sizes 0.5 mm, 0.75 mm and 1 mm are considered, whereas a Power Law rheological model is used for the fluid phase description. The EE approach implemented herein applies the Kinetic Theory of Granular Flow (KTGF) in ANSYS Fluent® and accounts for the particle size differences by representing them as different phases within the computational domain. With the LE approach, we employ the Dense Discrete Phase Model (DDPM) and capture this difference with the aid of a size distribution model (the Rosin-Rammler model). The findings of our computational experiments show considerable differences in key variables (the pressure drop, and particle deposition tendencies) between monodispersed and polydispersed transport scenarios.

Keywords: Polydispersity, Cuttings Transport, Discrete Phase Model, Rosin-Rammler

Highlights

- A comparison between monodispersed and polydispersed transport is presented.
- Considerable differences in cuttings transport velocity exist between the LE & EE method.
- Increased particle deposition is observed with monodispersed transport in this study.
- The pressure drop is overpredicted when monodispersity is assumed.

1. Introduction

The inherent complexity of cuttings transport and the numerous interdependent parameters simultaneously affecting wellbore cleaning remain subjects of concern in the drilling industry. Furthermore, slow drilling rates, pressure instabilities, excessive drill pipe torque, stuck drill pipe, and lost circulation are some of the specific operational challenges faced during wellbore cleaning (Epelle and Gerogiorgis, 2017, Zhu et al., 2019). These problems culminate to significantly increased capital and operating expenditure over the drilling and production time horizons. Thus, numerical tools and recent advances in computing developed by the process systems engineering community have been readily applied to understand cuttings transport phenomena with complex non-Newtonian fluids under unfavourable downhole conditions. Particularly, numerous studies that apply Computational Fluid Dynamics (CFD) for the description of annular multiphase (fluid-solid) transport of dense and dilute particulate mixtures have emerged over the past decade (Han et al., 2010; Duan et al., 2010; Zaisha et al., 2012; Demiralp, 2014; Akhshik et al., 2015; Rooki et al., 2015; Heydari et al., 2017; Epelle and Gerogiorgis, 2018a; 2018b; 2019; Huque et al., 2020; Yan et al., 2020). Recently, important new perspectives such as the application of ionic liquid-based muds (Rasool et al., 2021), modelling the settling behaviour of non-spherical particles using neural networks (Zhu et al., 2021), hydraulic pulsed jet technology (Wang et al., 2021), modelling cuttings lag distribution in directional wells (Naganawa, et al., 2021), the use of a grooved drill pipe for enhanced mud circulation and cuttings transport (Jiang et al., 2021) and the flow of fine solid particles (Movahedi and Jamshidi, 2021), have been considered in the field of cuttings transport.

The review article by Epelle and Gerogiorgis (2020) further provides a comprehensive analysis of past contributions in the field of cuttings transport from both experimental and modelling perspectives. However, a prevalent assumption in these studies is the existence of a monodispersed system of particles (both in terms of size and shape), which is never the case in real field operations; drill cuttings in the annulus are always of varying sizes and shapes. It is expected that the inclusion of this extra complexity (size polydispersity) will affect the resulting velocity field and particle concentration profiles obtainable. This is due to the multiple momentum transfer mechanisms (particle-fluid and particle-particle interactions) resulting from polydispersed transport scenarios. The future research directions proposed in this review (Epelle and Gerogiorgis, 2020) highlight the need for more work on polydispersity for a better understanding of cuttings transport; nonetheless, CFD studies accounting for polydisperse cuttings distribution are scarce, thus motivating this work herein. One of the few studies accounting for this phenomenon is that of Awad et al., (2021), in which a CFD model was applied to study polydispersed particle settling

behaviour in a shear-thinning fluid. They realised that cuttings with broad size distribution showed higher settling velocity than particles with a narrow size distribution. Yilmaz (2012) also implemented the Rosin-Rammler size distribution of the Discrete Phase Model (DPM) to analyse the average transport velocity of the cuttings bed at varying flowrates. They illustrated a negligible effect of the size distribution model on the transport velocities. This may be attributed to the fact that dilute particulate flow (< 12% particle volume fraction) was considered. Although not within the context of wellbore cleaning, multiphase particle-in-cell (MP-IPC) models have been developed to study polydispersed particle transport behaviour for hydraulic fracturing and fluidised bed applications by coupling a CFD model with the Discrete Element Method (Kim et al., 2020; Siddhamshetty et al., 2020; Verma and Padding, 2020; Wan et al., 2021).

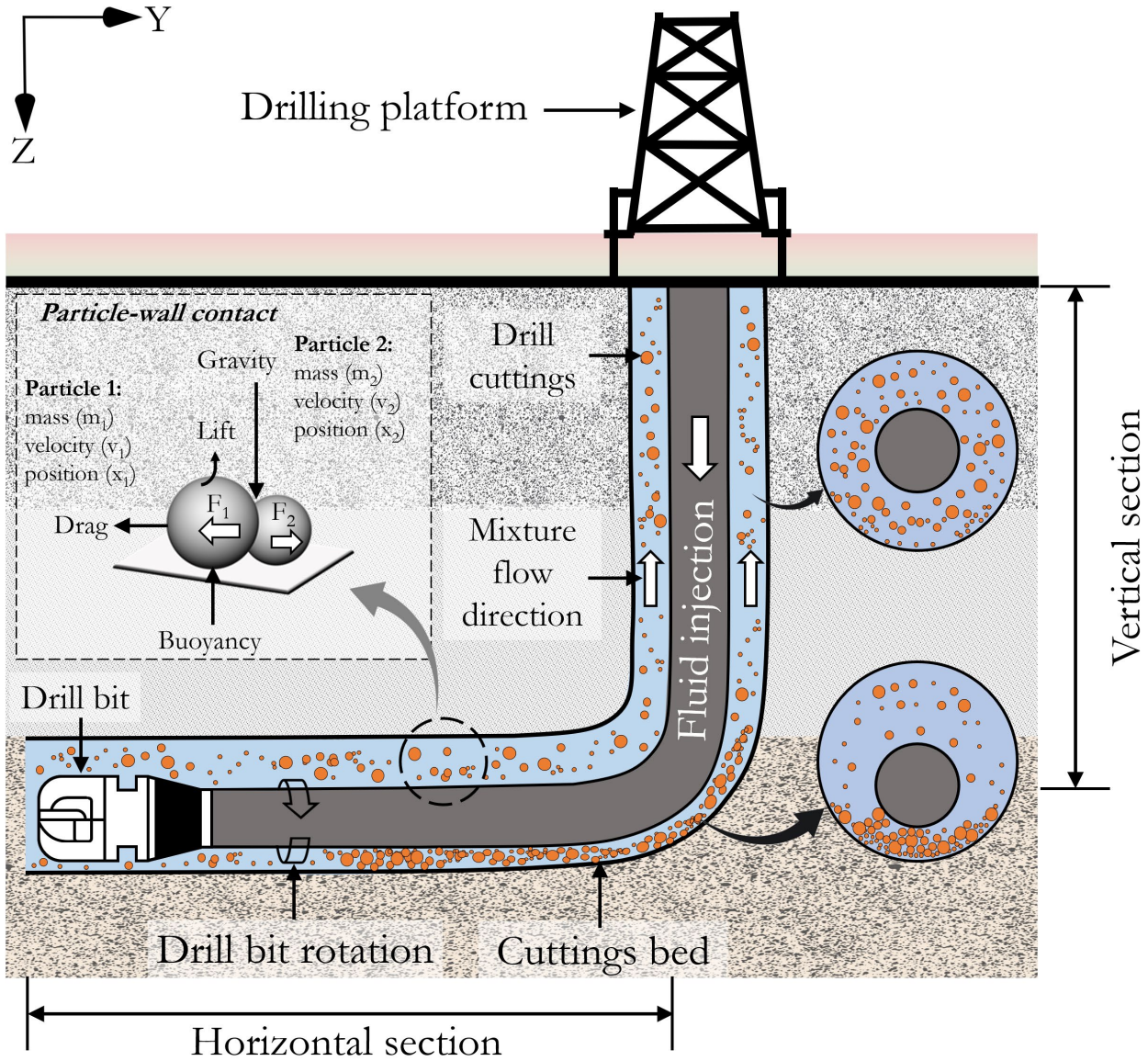

Figure 1: Evolution of rock cuttings during drilling operations.

In this study, polydisperse spherical particulate systems are examined using the Eulerian-Eulerian (EE) and Lagrangian-Eulerian (LE) modelling approaches in the context of wellbore cleaning operations in the drilling industry. To the best of the authors' knowledge, this is the first study to analyse the impact of particle polydispersity using both models in the context of annular cuttings transport for wellbore cleaning operations. The particle sizes considered here are between 0.0005 m and 0.001 m, whereas a Power Law rheological model is used for the fluid phase description. The EE approach implemented herein applies the Kinetic Theory of Granular Flow (KTGF) in ANSYS Fluent® and takes the particle size differences into consideration by representing them as different phases within the flow domain. In addition, the LE approach (employing the Dense Discrete Phase Model – DDPM) represents this difference with the aid of a size distribution model (the Rosin-Rammler model). The work presented herein is a continuation of our previous research efforts on the impact of particle sphericity (Epelle and Gerogiorgis, 2018b); albeit with a current focus on particle polydispersity using an already validated CFD model.

The results of the polydisperse system are presented in terms of the cuttings velocity profiles and the cuttings concentration along the annulus, and these are comparatively analysed with a monodispersed system. We consider this comparison to be another element of novelty in this work. The findings of our computational experiments show that neglecting the size disparity in the system may lead to severe under/overestimation of key variables such as the pressure drop, and the extent of particle deposition; thus, leading to decreased model performance. Incorporating polydispersity is a necessary step towards improving the predictive performance of CFD models in wellbore cleaning operations. It is also worth mentioning that annular flow transport conditions with polydisperse particles exist in numerous industrial settings (food processing, pulp and paper, mining and other slurry transport processes) (Dewangan, 2021). Thus, the findings presented herein have extended applicability and relevance to such scenarios.

2. Methodology & Model Description

In this study, the EE model is implemented as the first case study for describing annular multiphase flows as shown in Figs. 1 and 2. This model accounts for the particles of different sizes by treating them as separate continuous phases that interact with the non-Newtonian drilling mud via the interphase momentum exchange coefficient. The limitation of this continuum assumption is that the kinematic and discrete behaviours of the particles are not explicitly accounted for (Epelle and Gerogiorgis, 2017). However, the implementation of KTGF enables the estimation of these kinematic properties via closure models. Hence, for each particulate phase considered in this study,

we apply closure models for the granular viscosity, granular bulk viscosity, solid pressure, radial distribution and elastic modulus, respectively in ANSYS Fluent®.

Conversely, the LE model applied herein utilises statistically computed particle trajectories coupled with an Eulerian description of the fluid phase. The Dense Discrete Phase Model (DDPM) of ANSYS Fluent® is applied in this study, given its ability to model high particle loading in the annulus (ANSYS Fluent, 2017). Compared to the DPM, DDPM is more suitable in this regard. In describing the particle size variability, the Rosin-Rammler size distribution is implemented (parameters shown in Table 1). The stepwise procedure adopted in this work is shown in Fig. 3. Although the LE model is more computationally expensive than the EE model (up to 2 times the computational time required for the EE model), a better description of the particulate phase motion in the Lagrangian reference frame can be obtained. Further differences between the LE and EE modelling methods for multiphase flows are covered in Epelle and Gerogiorgis (2018a; b) and Subramaniam (2013).

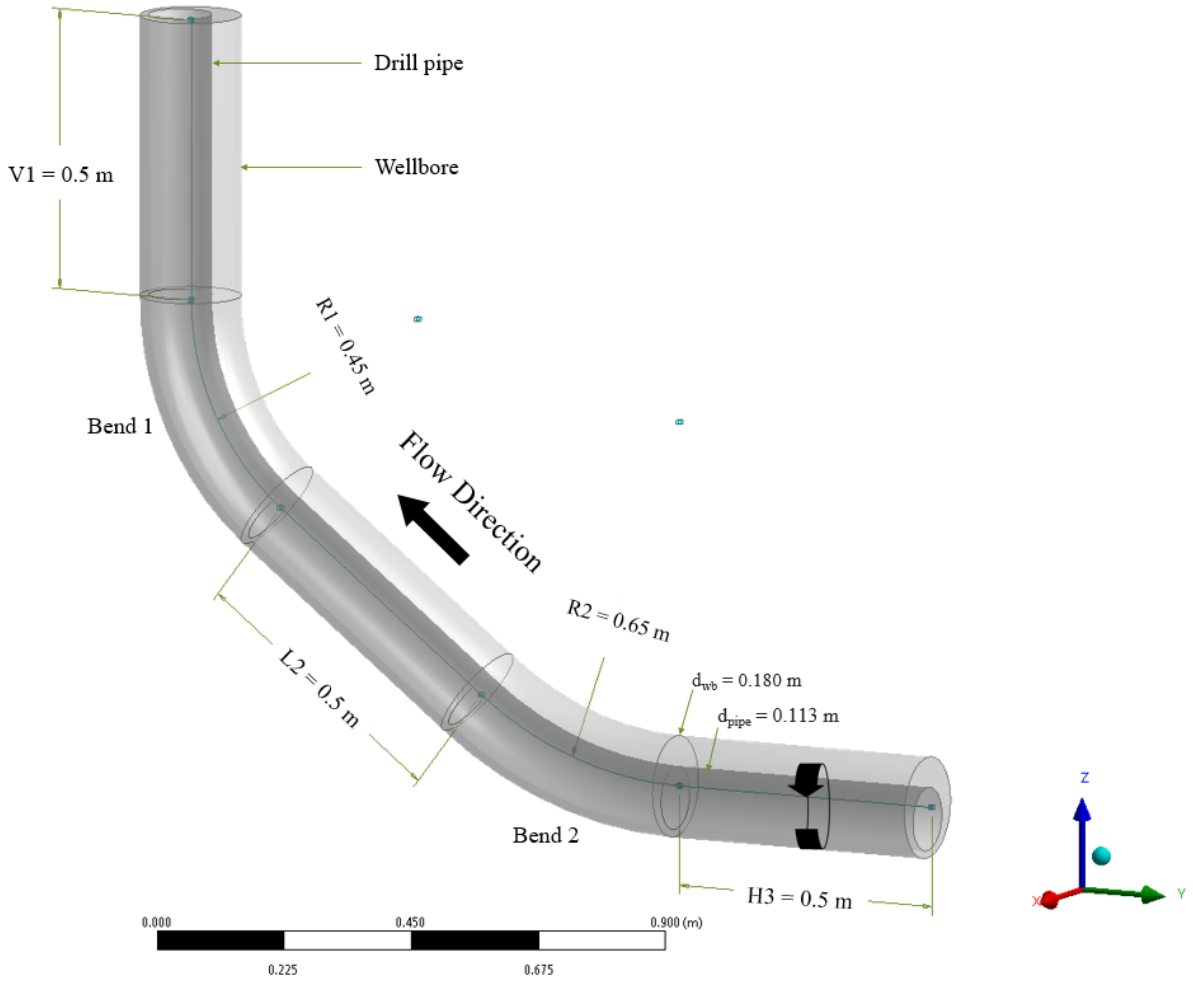

Figure 2: Annular flow domain.

The computational domain (Fig. 2) was constructed to model wellbore trajectories obtainable in deviated drilling operations, consisting of horizontal, inclined and vertical sections. Discretising the domain with hexahedral elements resulted in a mesh with 665,600 elements, optimal orthogonality, aspect ratio and skewness factors; this yielded grid-independent results; further mesh refinement did not produce a significant change in the results (Fig. 5). Table 1 describes the input parameters and boundary conditions utilised in this simulation; whereas, the set parameters and settings adopted are described in Table 2.

Table 1: Simulation input parameters and boundary conditions.

	EE model	**LE model**
Computational geometry		
Drill pipe diameter, d_c (m)	0.113	0.113
Casing diameter, d_{dp} (m)	0.180	0.180
Total length, L (m)	2.340	2.340
Fluid properties		
Composition	0.5% CMC solution	0.5% CMC solution
Fluid density, ϱ_l (kg.m^{-3})	1,000	1,000
Yield stress, τ_0 (Pa)	0	0
Consistency index, K (Pa.s^n)	0.524	0.524
Flow behaviour index, n	0.60	0.60
Particle properties		
Cuttings density, ϱ_p (kg.m^{-3})	2,800	2,800
Sphericity, ψ	1.00	1.00
Cuttings diameter, d_p (mm) & Rosin-Rammler parameters for the LE model	0.50 (d_{p1}), 0.75 (d_{p2}), 1.00 (d_{p3})	Min. d_p = 0.5; max. d_p = 1; mean d_p = 0.75; spread parameter = 3.368; number of diameters = 3
Drilling variables		
Cuttings inlet velocity, v_p (m.s^{-1})	0.25	0.25
Cuttings inlet volume fraction (-)	0.15 (d_{p1}), 0.2 (d_{p2}), 0.15(d_{p3})	0.50
Drill mud (fluid) circulation velocity, v_l (m.s^{-1})	1.50	1.50
Wellbore eccentricity, e	0.60	0.60
Drill pipe rotation (rpm)	100	100

Table 2: Simulation setup.

Property	Details	Rationale
Software used	ANSYS Fluent® (v 17.1)	License availability
Precision level	Double precision	Increased accuracy and the avoidance of floating-point errors.
Computer specifications	16 cores (2.4 GHz Intel®-Xenon® CPU processor) and 64 GB of RAM; Scientific Linux 7 Operating System	Available computing resource chosen to ensure speedy computations, and short queuing times (by the super-computing scheduler) per batch job submission.
Transient formulation	First-Order and Second-Order Implicit	Once stability is attained with 1st order, the simulation can be changed to 2nd order for increased accuracy.
Model used	Eulerian-Eulerian (EE) & Lagrangian-Eulerian (LE) with steady particle tracking using the DDPM model; turbulent models.	Robustness of multiphase flow models, and computational cost. A preliminary assessment of the turbulent models in ANSYS Fluent®, showed better stability of the *Realisable k-ε* model for the EE simulations and *Standard k-ω* for the LE simulations, respectively.
Mesh	665,600 hexahedral elements	Optimised mesh resolution to guarantee grid independence; skewness, orthogonality and aspect ratio were also monitored to ensure numerical stability.
Domain orientation	Horizontal, inclined & vertical	To simulate attainable geometries in extended drilling.
Pressure-velocity coupling	Semi-Implicit Method for Pressure Linked Equations (SIMPLE algorithm)	Numerical stability; and industry-standard (popularly used) for multiphase flow simulations.
Spatial discretisation (Gradient)	Least Squares Cell-Based	Computationally less expensive and accurate compared to node-based methods.

Spatial discretisation (Momentum)	QUICK (Quadratic Upstream Interpolation for Convective Kinematics)	
Spatial discretisation (Volume fraction)	QUICK	
Spatial discretisation (Turbulent kinetic energy)	QUICK	Adaptability to hexahedral meshes (Epelle and Gerogiorgis, 2018); it also applies an efficient weighted combination of the robust 2nd order upwind scheme and central interpolation of the variables, for increased accuracy and numerical stability in ANSYS Fluent®.
Spatial discretisation (Specific dissipation rate)	QUICK	
Stopping/convergence criteria (tolerance)	Absolute tolerance = 10^{-3}	Sufficient to guarantee simulation accuracy.
Solution controls (Pressure)	0.7	
Solution controls (Density)	1.0	
Solution controls (Body forces)	1.0	
Solution controls (Momentum)	0.3	These were tuned for numerical stability of the computations.
Solution controls (Volume fraction)	0.2	
Solution controls (Granular temperature)	0.2	
Solution controls (Turbulent kinetic energy)	0.8	

Solution controls (Specific dissipation rate)	0.8	
Solution controls (Turbulent viscosity)	1.0	
Initialisation method	Hybrid	Applies boundary interpolation methods and the solution to the Laplace's equation to determine the velocity and pressure fields. Simple to use and robust.
Time step (sec)	0.00005 - 0.0005	Chosen to guarantee numerical stability of the simulations.
Run time (sec)	5 - 12 sec	Sufficient to allow exit of all injected particles from the inlet and ensure statistically stationary state.
Extrapolate variables	Yes	Increased computational efficiency via the use of predicted solution variables of the next time step as the initial guesses for that time step.
Data sampling for time statistics	Yes	To enable ANSYS Fluent® compute the time average (mean) of the instantaneous values and root-mean-squares of the fluctuating values sampled during the calculation.
Auto-save time steps and solution history	Every 500 timesteps	Optimised saving frequency for good insight into flow dynamics while maintaining good file size management and storage.
Maximum iterations per timestep	100	This was chosen to ensure sufficient number of iterations for convergence at each timestep of the simulation.
Total number of timesteps	>10,000	Long enough to yield accurate and analysable results; the fluid-particle mixture had traversed the whole domain from the inlet to outlet multiple times.

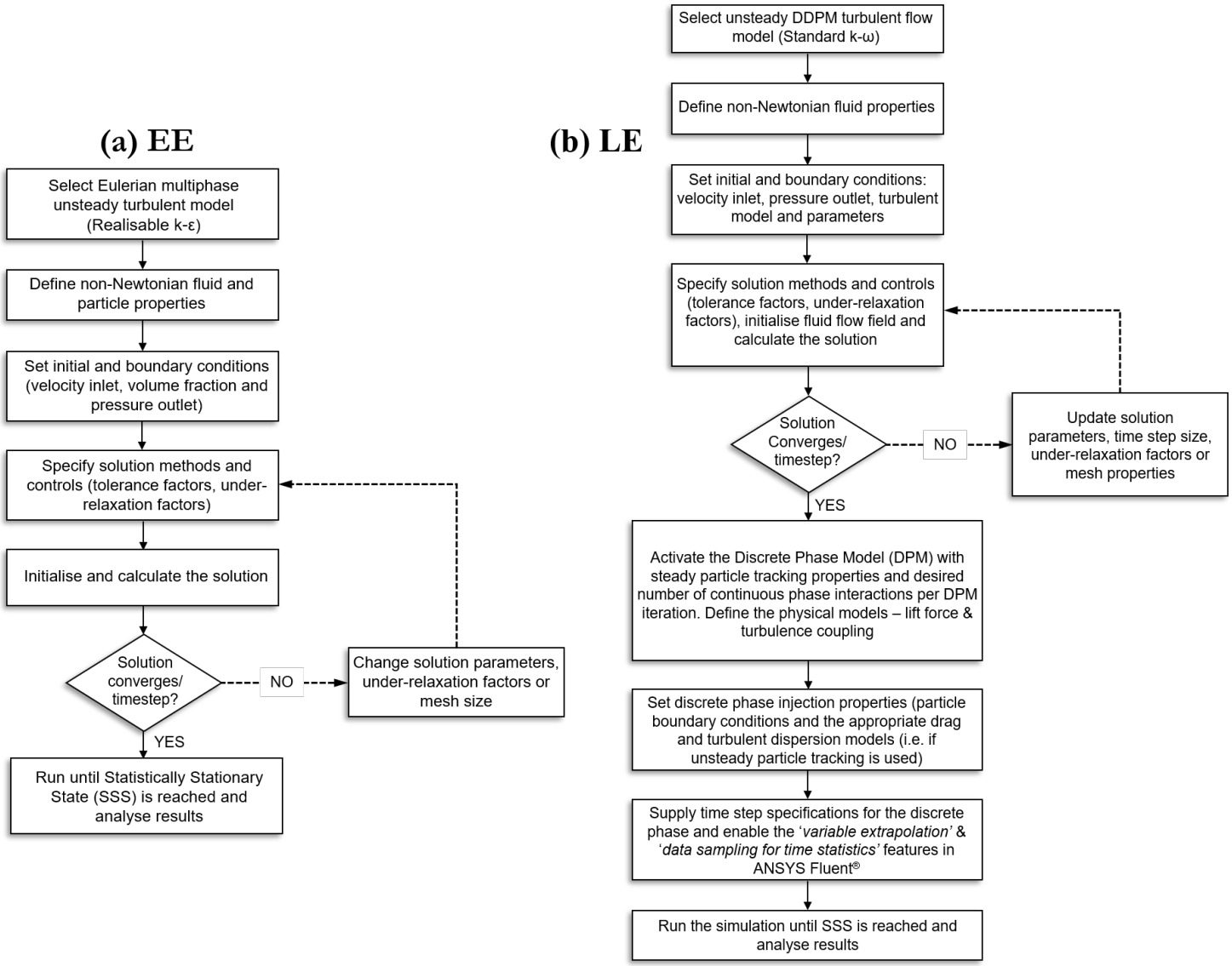

Figure 3: Simulation methodology for the EE and LE model.

2.3 Mathematical formulation of the EE model

2.3.1 Continuity

The volume fraction of each phase is calculated from the continuity equation:

$$\frac{1}{\rho_{rs}}\left(\frac{\partial}{\partial t}(\alpha_s\rho_s) + \nabla\cdot(\alpha_s\rho_s\vec{v}_s) = \sum_{l=1}^{n}(\dot{m}_{ls} - \dot{m}_{sl})\right) \quad (1)$$

2.3.2 Fluid-Fluid momentum equation

$$\frac{\partial}{\partial t}(\alpha_l\rho_l\vec{v}_l) + \nabla\cdot(\alpha_l\rho_l\vec{v}_l\vec{v}_l) = -\alpha_l\nabla p + \nabla\cdot\bar{\bar{\tau}}_q + \alpha_l\rho_l\vec{g} + \sum_{s=1}^{N}(K_{ls}(\vec{v}_l - \vec{v}_s) + \dot{m}_{ls}\vec{v}_{ls} - \dot{m}_{sl}\vec{v}_{sl}) + (\vec{F}_l + \vec{F}_{lift,l} + \vec{F}_{vm,l} + \vec{F}_{td,l}) \quad (2)$$

2.3.3 Fluid-Solid momentum equation

$$\frac{\partial}{\partial t}(\alpha_s\rho_s\vec{v}_s) + \nabla\cdot(\alpha_s\rho_s\vec{v}_s\vec{v}_s) = -\alpha_s\nabla p - \nabla p_s + \nabla\cdot\bar{\bar{\tau}}_q + \alpha_s\rho_s\vec{g} + \sum_{l=1}^{N}(K_{ls}(\vec{v}_l - \vec{v}_s) + \dot{m}_{ls}\vec{v}_{ls} - \dot{m}_{sl}\vec{v}_{sl}) + (\vec{F}_s + \vec{F}_{lift,s} + \vec{F}_{vm,s} + \vec{F}_{td,s}) \quad (2)$$

Where $\vec{v}_s$ is the velocity of the solid phase, $\vec{v}_l$ is the velocity of the liquid phase, α_s is the volume fraction of the solid phase, ρ_s is the density of the solid phase, ρ_l is the liquid phase density, $\dot{m}_{ls}$ and $\dot{m}_{sl}$ characterise the mass transfer between solid and liquid phases respectively, $\vec{v}_{ls}$ and $\vec{v}_{sl}$ are the interphase velocities, g is the acceleration due to gravity, ρ_{rs} is the phase reference density, $\vec{F}_s$ is an external body force, $\vec{F}_{lift,s}$ is the lift force, $\vec{F}_{vm,s}$ is the virtual mass force and $\vec{F}_{td,s}$ is the turbulent dispersion force (applicable to turbulent flows only). The equations for the force terms, including the lift force, are detailed in the Fluent theory manual (ANSYS Fluent, 2017).

2.3.4 Fluid-Solid exchange coefficient

In the Syamlal-O'Brien (SO) model (Syamlal and O'Brien, 1987), the fluid-solid exchange

coefficient is defined as:

$$K_{sl} = \frac{3\alpha_s \alpha_l \rho_l}{4 v_{r,s}^2 d_s} C_D \left(\frac{Re_s}{v_{r,s}}\right) |\vec{v}_s - \vec{v}_l| \tag{3}$$

The drag function (C_D) in Eq. 3 has a form derived by Dalla Valle (1943); Re_s is the particle Reynolds number,

$$C_D = \left(0.63 + \frac{4.8}{\sqrt{\frac{Re_s}{v_{r,s}}}}\right)^2 \tag{4}$$

$$Re_s = \frac{\rho_l d_s |\vec{v}_s - \vec{v}_l|}{\mu_l} \tag{5}$$

$v_{r,s}$ is the terminal velocity correlation for the solid phase and μ_l the viscosity of the liquid phase.

$$v_{r,s} = 0.5\left(A - 0.06Re_s + \sqrt{(0.06Re_s)^2 + 0.12Re_s(2B - A) + A^2}\right) \tag{6}$$

Where

$$A = \alpha_l{}^{4.14} \tag{7}$$

and

$$B = 0.8\alpha_l{}^{1.28} \; for \; \alpha_l \leq 0.85 \; and \; B = 0.8\alpha_l{}^{2.65} \; for \; \alpha_l > 0.85 \tag{8}$$

2.3.5 Closures

Closure models of relevant flow properties and effects, such as the granular temperature and viscosity, solids and frictional pressure also have to be accounted for.

2.3.5.1 Granular viscosity – Syamlal et al. (1993)

$$\mu_s = \frac{\alpha_s d_s \rho_s \sqrt{\Theta_s \pi}}{6(3 - e_{ss})}\left[1 + \frac{2}{5} g_{0,ss} \alpha_s (1 + e_{ss})(3e_{ss} - 1)\right] \tag{13}$$

2.3.5.2 Granular bulk viscosity – Lun et al. (1984)

$$\lambda_S = \frac{4}{3}\alpha_S^2 \rho_S d_S g_{0,SS}(1+e_{SS})\left[\frac{\Theta_S}{\pi}\right]^{1/2} \tag{14}$$

2.3.5.3 Frictional Viscosity – Schaeffer (1987)

At high particle volume fractions, the frictional force between particles may have a significant effect on particle behaviour:

$$\mu_{S,fr} = \frac{p_S \sin\phi}{2\sqrt{I_{2D}}} \tag{15}$$

Where p_S is the solids pressure, ϕ is the angle of internal friction and I_{2D} is the second invariant of the deviatoric stress tensor.

2.3.5.4 Frictional Pressure – Johnson and Jackson (1987)

$$P_{friction} = Fr\frac{(\alpha_s - \alpha_{s,\min})^n}{(\alpha_{s,max} - \alpha_s)^p} \tag{16}$$

Where coefficient $Fr = 0.05$, $n = 2$ and $p = 5$

2.3.5.4 Solids Pressure – Lun et al. (1984)

$$p_s = \alpha_s \rho_S \Theta_S + 2\rho_S(1+e_{SS})\alpha_S^2 g_{0,SS}\Theta_S \tag{17}$$

Where e_{SS} is the coefficient of restitution for particle collisions; $g_{0,SS}$ is the radial distribution function and Θ_S is the granular temperature

2.3.5.5 Radial Distribution – Lun et al. (1984)

$$g_{0,SS} = \left[1 - \left(\frac{\alpha_s}{\alpha_{s,max}}\right)^{\frac{1}{3}}\right]^{-1} \tag{18}$$

The radial distribution function is a correction factor that modifies the probability of collisions between particles in the computational domain when the particulate volume fraction of the cuttings becomes dense. It may also be understood as the non-dimensional distance between spherical particles (ANSYS Fluent, 2017).

2.3.5.6 Granular temperature transport equation (algebraic formulation)

$$0 = \left(-p_S\bar{\bar{I}} + \bar{\bar{\tau}}_s\right):\nabla\vec{v}_s - \gamma_{\Theta S} + \phi_{ls} \tag{19}$$

$\left(-p_s\bar{\bar{I}} + \bar{\bar{\tau}}_s\right) : \nabla\vec{v}_s$ is the generation of energy by the solid stress tensor; γ_{Θ_S} is the collisional dissipation of energy and ϕ_{ls} is the energy exchange between the fluid and solid phases.

2.3.5.7 Collisional dissipation of energy – Lun et al. (1984)

$$\gamma_{\Theta S} = \frac{12(1-e_{ss}^2)g_{0,SS}}{d_S\sqrt{\pi}}\rho_S\alpha_s^2{\Theta_S}^{3/2} \tag{20}$$

The collisional dissipation of energy represents the rate of kinetic energy dissipation within the particles in the domain due to collision with other particles (particle-particle interactions). Without the inclusion of this parameter, the change in particle momentum due to collisions with surrounding particles (in dense granular flows) cannot be captured in the Eulerian-Eulerian model. This constitutive relation allows for an accurate representation of the settling and central-axial transport tendencies of the particles under high particle loading in the annulus.

2.4 Mathematical formulation of the LE model

The particle trajectory of the discrete phase is computed by integrating the force balance on the particle in the Lagrangian reference frame. This force balance can be defined as:

$$\frac{d\vec{v}_s}{dt} = F_D(\vec{v}_l - \vec{v}_s) + \frac{\vec{g}(\rho_s - \rho_l)}{\rho_s} + \vec{F} \tag{21}$$

Where $\vec{F}$ is an additional force consisting of the lift, and other negligible forces (virtual mass and pressure gradient forces, which are not necessary when the density of the fluid is much lower than the density of the particles), $F_D(\vec{v}_l - \vec{v}_s)$ is the drag force per unit mass, $\overrightarrow{v_l}$ is the fluid velocity, μ_l is the molecular viscosity of the fluid, ρ_l is the fluid density, ρ_s is the density of the particle, and d_s is the particle diameter. Re_{ss} is the relative Reynolds number, defined as:

$$F_D = \frac{18\mu_l}{\rho_s {d^2}_s}\frac{C_D Re_s}{24} \tag{22}$$

$$Re_{ss} \equiv \frac{\rho_l d_s|\vec{v}_s - \vec{v}_l|}{\mu_l} \tag{23}$$

When a moving reference frame is involved, the additional force term incorporates the forces on particles due to drill pipe rotation. For rotation about the z-axis, the forces in Cartesian x and y coordinates can be written as:

$$\left(1 - \frac{\rho_l}{\rho_s}\right)\Omega^2 x + 2\Omega\left(v_{s,y} - \frac{\rho_l}{\rho_s}v_{l,y}\right) \tag{24}$$

Where $v_{s,y}$ and $v_{l,y}$ are the particle and fluid velocities in the Cartesian y-direction, Ω is the RPM, and

$$\left(1-\frac{\rho_l}{\rho_s}\right)\Omega^2 y + 2\Omega\left(v_{s,x}-\frac{\rho_l}{\rho_s}v_{l,x}\right) \tag{25}$$

Where $v_{s,x}$ and $v_{l,x}$ are the particle and fluid velocities in the Cartesian x-direction, respectively.

A full description of the LE (DDPM) model (including the mass and momentum equations) can be found in ANSYS Fluent's® (2017) theory guide.

4. Results and Discussion

4.1 Grid independence and experimental validation

The mesh properties discussed in Table 2, are depicted in Fig. 4a. This consists of 80 divisions around the circumference and 20 divisions in the radial direction, yielding a minimum orthogonality of 0.73, and a maximum skewness factor of 0.49. These parameters were sufficient to yield grid independence and accuracy of the performed computations. Furthermore, the pressure drop (resulting from the fluid and particle velocities and their respective volume fractions), shows good agreement with the experimental data of Sorgun (2010), as shown in Fig. 4b; thus, demonstrating the reliability of the performed computations in this work. The EE model was used for the validation presented herein to reduce the computational cost. Further validation results can be found in Epelle and Gerogiorgis (2017; 2018a; 2018b).

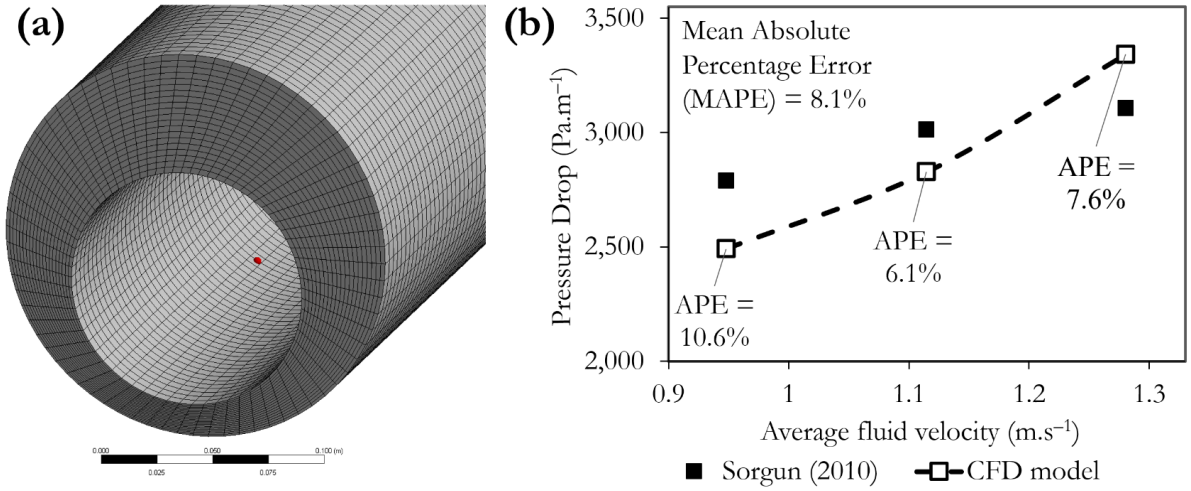

Figure 4: Mesh quality and validation of methodology; experimental data taken from Figure 5.4 of Sorgun (2010).

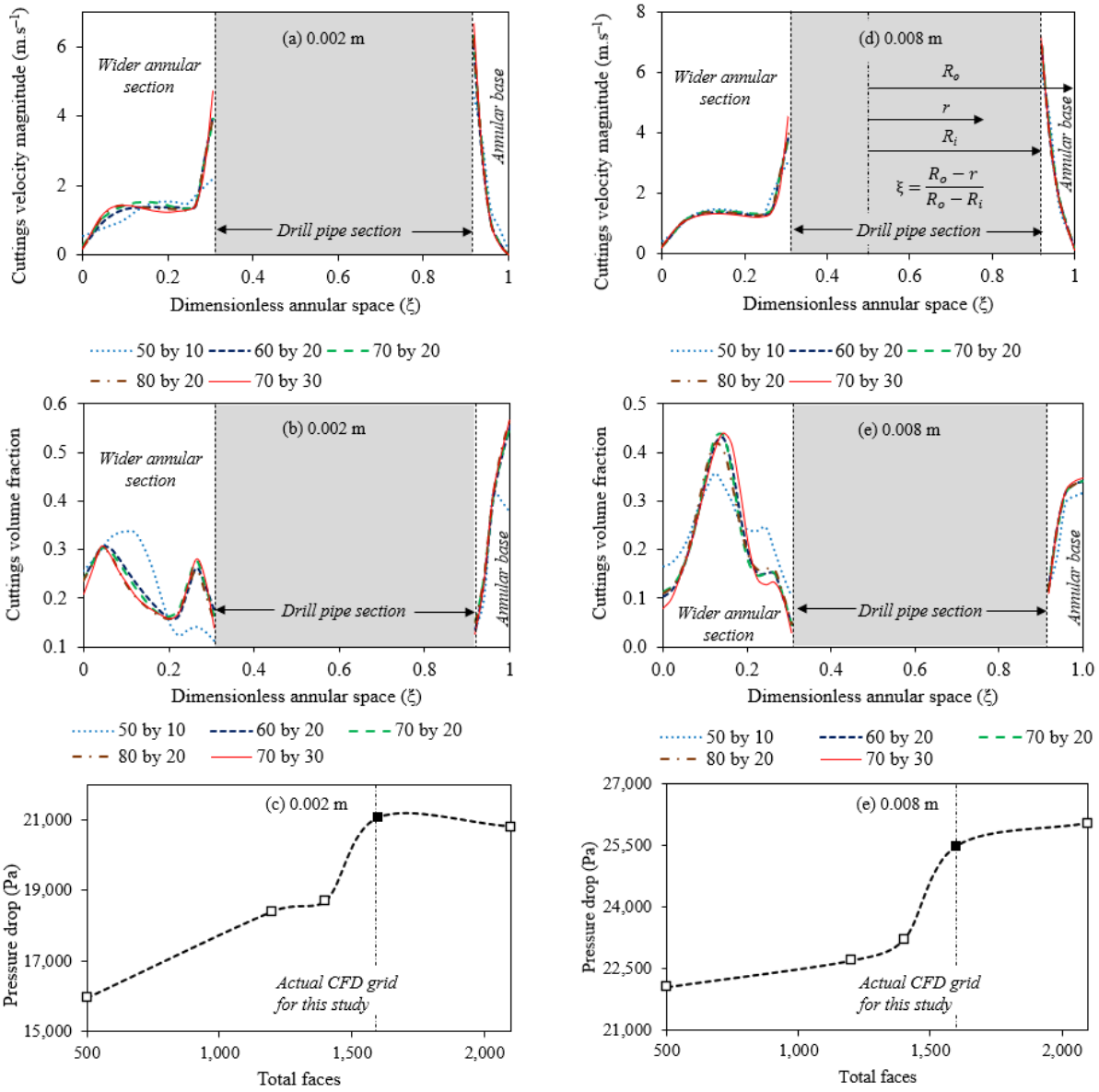

Figure 5: Mesh independence study (Epelle and Gerogiorgis, 2018b).

4.2 Analysis of mean particle volume fraction in the entire annulus

The cuttings volume fractions for the respective particulate phases of the EE-poly model and the LE-poly model are shown in Fig. 6 (a-d). Generally, the 0.75 mm particles occupy a significant portion of the annulus, with higher averaged volume fractions observed. This is attributable to its relatively higher inlet volume fraction compared to the other particle sizes (Table 1). However, it can also be observed that the concentration of the smallest particles (0.5 mm) at the annular base is highest; although with some unoccupied regions in the upper/wider annular section. Thus, in a polydispersed scenario, smaller particles can cause some transport difficulties. It is worth highlighting that the maximum concentration (denoted as the dark red region) has a volume

fraction of 0.25, and does not reflect a packed bed (volume fraction > 0.63 in ANSYS Fluent®). The LE model on the other hand shows a rather unified bulk movement of the particles (although with some faint red regions). This observation can be attributed to the implementation of a size distribution model in the flow domain, compared to the EE scenario in which the particulate phases are separate but interacting (Pang et al., 2018). Fig. 6e shows a monodispersed transport condition, in which there is a significant deposition of the 0.75 mm particles, with the packing limit of 0.63 reached; this observation (increased deposition of uniformly-sized particles) was also pointed out by Awad et al. (2021). This may be explained by the fact that the co-existence of large and small particles, reduces the shear rate of the non-Newtonian drill mud in the lower annular region; thus, yielding a better carrying capacity compared to the monodispersed scenario in this work. However, it should be mentioned that the validity of this explanation is limited to the narrow particle size distribution employed herein. Larger size distributions (where the ratio of the largest particle's diameter to the smallest particle's diameter is >> 2) require further investigation.

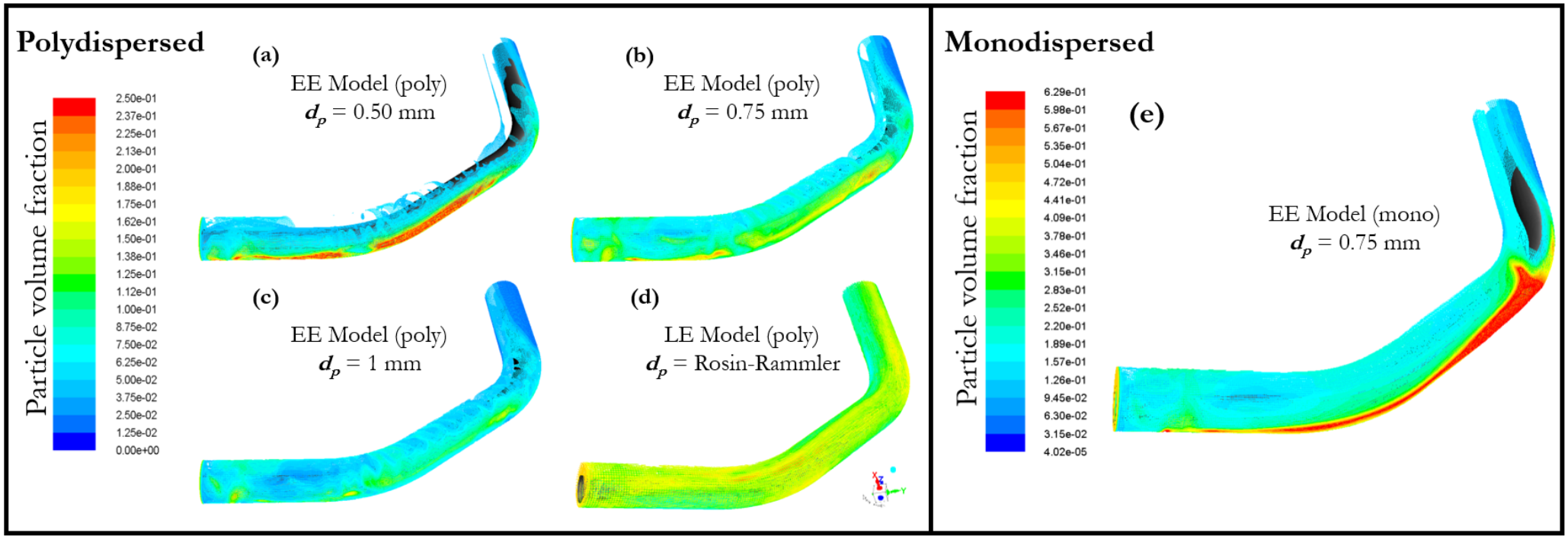

Figure 6: Time-averaged contours of particle volume fraction for the LE and EE models.

4.3 Analysis of mean particle velocity contours of the entire annulus

On analysing the velocity contour plots for the different particle sizes of the EE-poly model, no significant differences in the velocity magnitude were observed; thus, single-particle velocity plots of the EE-poly models are compared with the EE-mono and LE model, as shown in Fig. 7. However, both plots similarly portray the wider annular sections, as the regions of high velocity; this observation is attributable to the eccentricity of the domain. Furthermore, the velocities in the horizontal-to-inclined annular region of the EE models show significantly higher values compared to the LE model. The inherent treatment of the solid phase as a continuous phase and the possible overestimation of its velocity is the likely reason for this observation when compared to the LE model, in which the original discrete behaviour of the particles is preserved. Results of the EE-mono model (Fig. 7c) show a more pronounced region of low velocity (dark-blue colour) in the narrower annular space compared to the EE-poly model. This corresponds to the increased cuttings volume fraction observed in Fig. 6. It is also worth mentioning that the EE model showed significantly better numerical stability with the specified rotary boundary condition at the drill pipe walls compared to the LE model. Hence, the rotational effect was only gradually applied (and repeatedly increased) to the LE model to ensure stability. This difference in the addition of the extra velocity component (via rotation) may have also resulted in the higher velocities observed in the EE model.

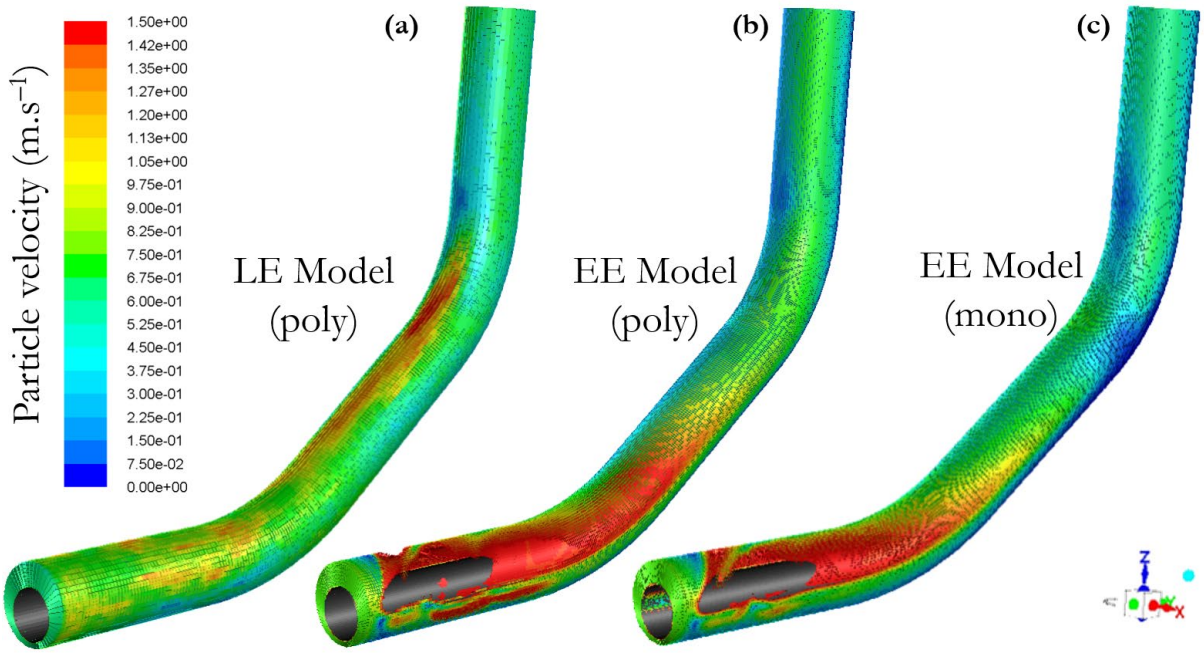

Figure 7: Mean particle velocity contours for the LE and EE models.

4.4 Analysis of mean particle velocity contours on selected planes and line segments

To further understand the velocity variation of the EE and LE models under both monodispersed and polydispersed scenarios, particle velocity contours at the outlet of the annulus (along the X-Y plane) are analysed as shown in Fig. 8 (a-c). The appearance of a shifted high-velocity region (to the right) for all scenarios is indicative of the rotating boundary condition applied to the drill pipe, in the simulation setup (Tables 1 and 2). The monodispersed scenario (Fig. 8c) particularly shows a wider high-cuttings-velocity region at the annulus' outlet. An analysis of the fluid and particle velocities along the line segment AB (Fig. 8d) at the annulus outlet is also performed and plotted against the dimensionless annular distance (β), as shown in Fig. 9. It can be observed that there is considerable cuttings lag (relative to the fluid velocity) in the LE model; whereas, both fluid and particle velocities overlap in the EE-mono and EE-poly models. Hence, indicating that the particles assume the fluid's turbulent velocity more readily with the EE models than the LE model. This is unlikely to be the case at other regions of the annulus (especially at regions of intense deposition) and before a statistically stationary state is achieved. Epelle and Gerogiorgis (2018a) have shown the possibility of obtaining significant slip velocities when using the EE model.

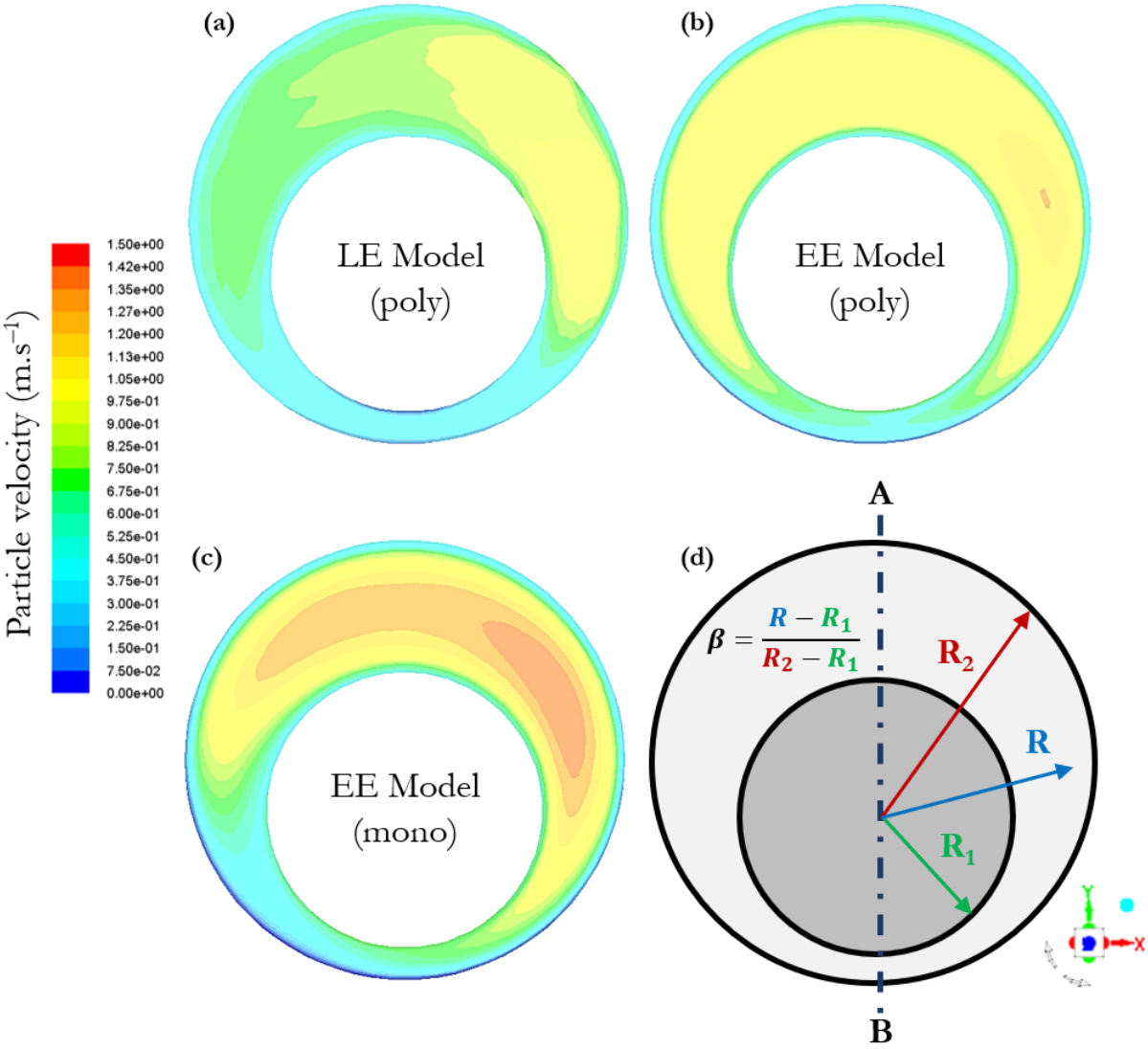

Figure 8: Mean particle velocity contours for the LE and EE models at the outlet.

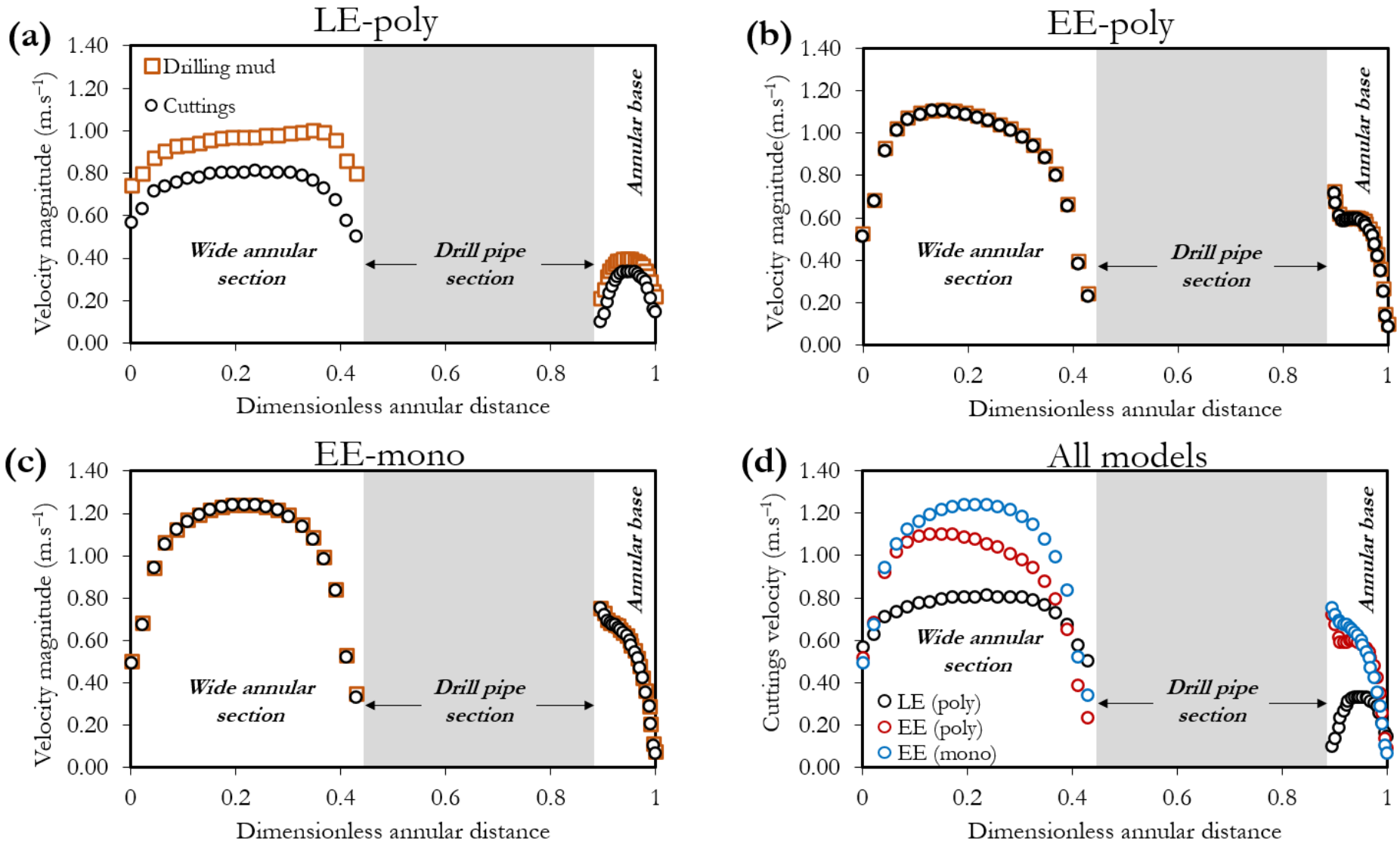

Figure 9: LE and EE analyses of particle velocity profiles along the line segment AB in Fig. 8.

Notwithstanding, Fig. 9 further demonstrates the differences between the treatment of the particulate phase by the LE and EE models. It is worth pointing out that, the wider region of the annulus (LE model – Fig. 9a) shows a considerable difference between fluid and particle velocities compared to the narrower region. This is because, the increased particle concentration in the lower/narrower region significantly impedes the bulk transport velocity of the fluid; compared to the wider region of lower particle concentration, in which there is freer fluid transport.

Fig. 9d illustrates the differences in cuttings transport velocity at the outlet for all 3 models applied. As observed, the monodispersed transport scenario shows a clearly higher particle velocity in the wider annular space than the polydispersed case. Contrary to this observation, the narrower annular region shows a reduced disparity between both velocities. Thus, it may be concluded that the effect of polydispersity when applying the EE model is more pronounced in the wider annular region. The LE model shows a further reduced peak velocity compared to both EE models; the treatment of the particulate phase as interpenetrating continua (by the EE model) implies that the particles more readily assume the fluid's velocity compared to a scenario where the force balance equations on the particles are directly computed (the LE model). Thus, the LE model may be considered a more realistic representation of the multiphase flow system. This indicates that the assumption of monodispersity is likely to yield significant overpredictions of the cuttings transport velocity and deposition tendencies. However, a more representative extent of this overprediction is better understood from the volume-averaged velocities across the entire flow domain, rather than the outlet alone. This volume-averaged analysis is presented subsequently in Section 4.6.

4.5 Analysis of particle diameter distribution of the LE model

Fig. 10, shows the contours of the particle diameter distribution in the flow domain at different time intervals. It can be observed that the larger 1-mm diameter particles mainly exist in the annulus at 1, 2 and 3 s of flow time. The other particle diameters (0.5 mm and 0.75 mm) are more predominant in the annulus at the 4^{th}, 5^{th}, and 6^{th} second. The particle diameter distribution in the first 3 s of flow time also demonstrates a somewhat swirly profile. This may be attributable to the drill pipe motion, which significantly affects larger particles (thus, aiding their transport) compared to smaller-sized particles, as shown by Epelle and Gerogiorgis (2018b). Thus, the smaller-sized particles are mainly transported by the axial fluid movement in the annulus.

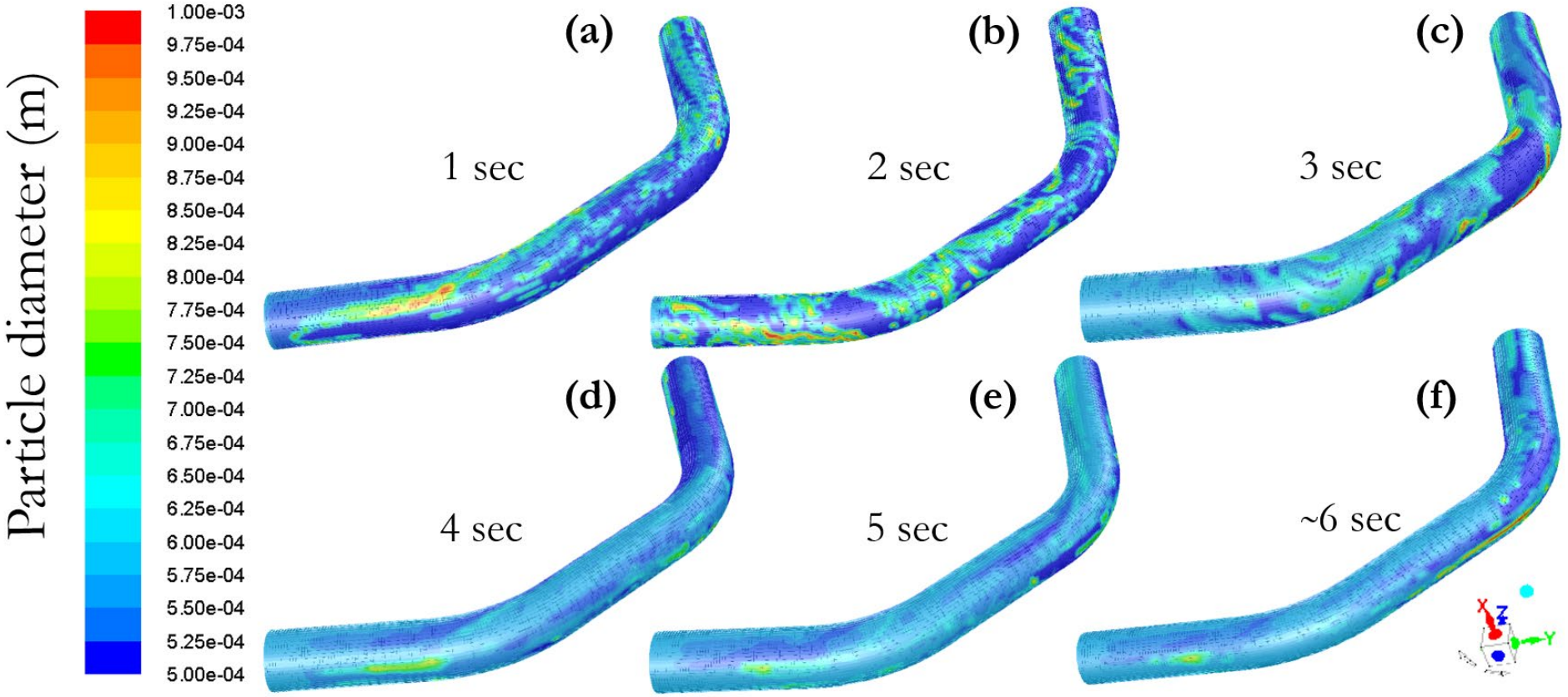

Figure 10: Particle diameter distribution at different flow times for the LE model.

4.6 Performance summary of multiphase flow models

Fig. 11 and Table 3 present a summary of the volume-averaged properties (over the entire computational domain) for the EE and LE models, respectively. It is worth mentioning that the LE model result is taken as the base value for comparing the results of the EE model; this is because of its more representative particle treatment method (the computation of actual particle trajectories), and its adaptability to a particle size distribution model (Subramaniam, 2013; Epelle and Gerogiorgis, 2018a). For reasons previously explained, a 27% overestimation of the velocity by the EE-poly model is observed; however, both EE models (mono and poly) show strong similarities in the velocity magnitude. The radial velocity components for all 3 models are similar; thus indicating that the axial and tangential velocities (of the LE and EE model) are the main contributors to the difference observed in the velocity magnitude.

Conversely, the EE models underpredict the volume fraction by approximately 25% as observed in Fig. 11a. This presented volume-averaged value for the EE model was also averaged over the 3 particle diameters. The slight dissimilarity observed in volume fraction (between EE-poly and LE-poly models) may be associated with the difference in the particle handling methods of both models (separate particulate phases vs. size distribution model). Also worth mentioning here, is the fact that the intense deposition with the monodispersed scenario (EE-mono) earlier observed in the volume fraction contour plots (Section 4.2) only translates to a slightly higher volume-averaged volume fraction, compared to the polydispersed scenario (EE-poly).

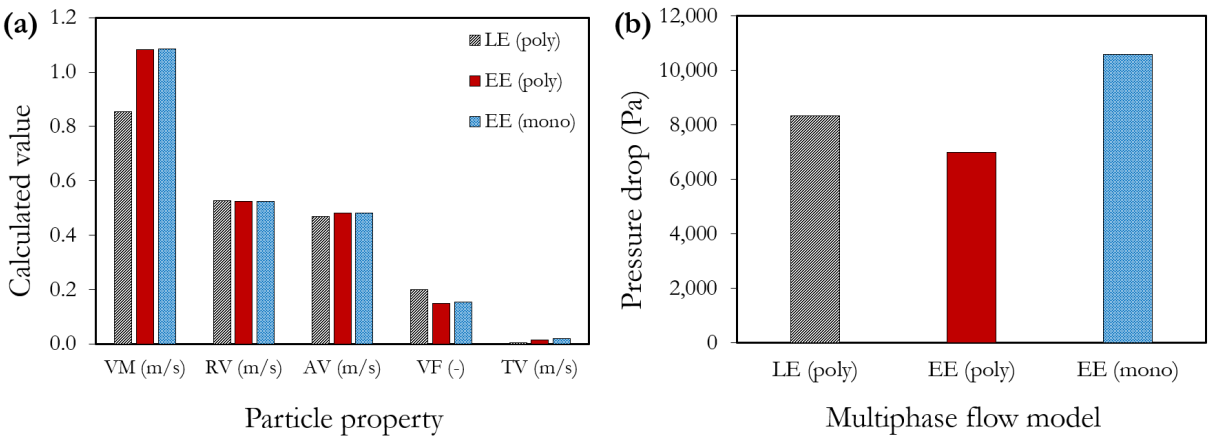

Figure 11: Velocity components and pressure drop for the EE and LE model: VM → velocity magnitude; RV → radial velocity; AV → axial velocity; VF → volume fraction; TV → tangential velocity.

Fig. 11b highlights the difference in the calculated pressure drop across the entire computation length for the EE and LE models. It can be observed that a difference of up to 1,300 Pa exists between the EE-poly and LE-poly model (19% overestimation); despite the higher travel velocities observed with the EE-poly model, the pressure drop is lower. This may be attributable to the more robust representation of the fluid-particle interactions by the LE model (via individually computed particle trajectories). The resulting pressure drop from such momentum exchange is likely to be greater compared to a scenario where constitutive relations (which often assume rapid/instantaneous attainment of the particle terminal velocity) are used, as is the case with the EE-poly model. Thus, the consumption of the fluid's momentum, via a relatively prolonged presence of the particles in the bulk transport region (before settling) is better captured by the LE model. This translates to the increased pressure drop observed and the reduced deposition seen with the LE model compared to the EE-poly. However, the monodispersed scenario reveals a significantly higher pressure drop than the polydispersed cases, which is most likely due to the heavily clogged regions of the annulus and the resulting increased fluid-particle friction. Thus, it may be argued that the resulting pressure drop is a complex interplay of depositional velocities, bulk particle transport, and increased fluid-particle friction. This is a further indication that the assumption of monodispersity in a polydispersed transport system, may yield an overestimation of the pressure drop required (as high as 51% in this work).

Table 3: Velocities and volume fractions of drilling mud and cuttings.

Model	**Volume-averaged velocities ($m.s^{-1}$)**					**Volume-averaged VF**
	Phases	VM	RV	TV	AV	
LE (poly)	Drilling mud	0.8738	0.5265	0.0051	0.4879	0.8014
	Cuttings	0.8530	0.5264	0.0031	0.4689	0.1986
EE (poly)	Drilling mud	1.0868	0.5257	0.0168	0.4880	0.8517
	0.0050 m cuttings	1.0850	0.5257	0.0166	0.4851	0.0439
	0.0075 m cuttings	1.0836	0.5256	0.0156	0.4823	0.0593
	0.001 m cuttings	1.0817	0.5253	0.0145	0.4792	0.0451
EE (mono)	Drilling mud	1.0873	0.5256	0.0203	0.4880	0.8447
	0.0075 m cuttings	1.0845	0.5254	0.0188	0.4823	0.1553

VM: Velocity magnitude; RV: Radial velocity; TV: Tangential velocity; Axial velocity; VF: Volume Fraction

An analysis of the turbulent properties for both EE models (mono- and polydispersed) shows striking similarities; however, the turbulent dissipation rate is the main exception (Table 4). In the monodispersed scenario, the rate of dissipation of the kinetic energy of turbulence is 1.68 times the polydispersed scenario. This faster dissipation translates to increased deposition velocity of the

monodispersed particles; whereas, the slower dissipation rate of the polydispersed scenario yields a sustained bulk transport of the particles by the drilling mud in the annulus. This can be observed in the contour plots of Fig. 6. A further plausible reason for the observed differences can be explained by considering the differences in the cumulative mass of 10 monodispersed and 10 polydispersed particles. Assuming the same density of particles, the cumulative mass of 10 monodispersed cuttings of 0.75 mm diameter is approximately 1.54 times that of a polydispersed scenario (distributed according to the inlet volume fractions shown in Table 1). This higher cumulative mass induces further dissipation of the turbulent kinetic energy (Epelle and Gerogiorgis, 2018a) of the fluid as shown in Table 4.

Table 4: Turbulence properties for the EE model.

Turbulent properties	EE (mono)	EE (poly)
Turbulent Kinetic Energy ($m^2.s^{-2}$)	0.115	0.118
Turbulent Intensity (%)	23.189	24.336
Turbulent Dissipation Rate (ε, $m^2.s^{-3}$)	12.118	11.675
Specific Dissipation Rate (ω, s^{-1})	1011.516	601.298
Turbulent viscosity ($kg.m^{-1}.s^{-1}$)	0.378	0.384
Effective viscosity ($kg.m^{-1}.s^{-1}$)	0.498	0.484
Turbulent Viscosity Ratio	3.785	3.961
Turbulent Reynolds Number	39.459	41.353

The computational effort required for the respective simulations is shown in Table 5. It is observed that the LE model requires a significantly higher duration to attain statistically stationary state. To attain numerical stability the timestep had to be changed periodically between 0.00005 and 0.0005 sec for the entire duration of the simulation.

Table 5: Approximate computational times.

Model	**Computational time (hours)**
EE-mono	24
EE-poly	96
LE-poly	168

5. Conclusions and Future Perspectives

This study has evaluated the influence of particle polydispersity on the cuttings transport efficiency in a deviated annulus and comparatively analysed the differences between the EE model (via KTGF) and the LE model (via DDPM). Presented velocity and particle concentration profiles

indicate that flow complexity will further increase due to multiple momentum transfer mechanisms (particle-fluid and particle-particle interactions) resulting from polydispersity. The findings of our computational experiments can be summarised as follows:

- Neglecting the size disparity in the system may lead to an overestimation of the depositional tendencies of the particles, and overall pressure drop; thus, leading to inaccurate predictions.
- From a computational cost perspective, the LE model required roughly 2 times the time and effort needed for the EE model.
- The numerical stability of the LE model proved sensitive to the rotational effect of the drill pipe.
- The monodispersed scenario yielded the highest particle transport velocity at the outlet and overall pressure drop, compared to the polydispersed scenarios (EE-poly and LE-poly).
- The monodispersed scenario also showed significant deposition tendencies compared to the polydispersed transport conditions, with lower deposition velocities.

The current work has shown that incorporating particle polydispersity is a necessary procedure towards improving the predictive performance of CFD models in wellbore cleaning operations. However, further work may consider the effect of polydispersity in both the particle size and sphericity. Although more computationally demanding, a wider particle size distribution covering both fine (<0.5 mm) and large (>3 mm) particle sizes is also worth investigating; such endeavours will be motivated by sound experimental measurements for model validation purposes. The assumption of uniform eccentricity in the flow domain applied herein may be improved upon in future studies. A longer annulus with changing eccentricities of the drillpipe relative to the wellbore will ensure a better representation of practical drilling scenarios.

It is also worth performing a comparative assessment of the predictive accuracies of different drag models (originally developed for Newtonian and non-Newtonian fluids), specifically for annular wellbore cleaning applications, where non-Newtonian drilling muds are used. This is because most of the drag models implemented in Fluent were originally developed for fluidized bed applications (gas-solid multiphase flows). Such endeavour will require some customization via user-defined functions in Fluent (for the specification of new drag models) or the use of a correction factor via a cell model approach (Kinaci, 2015; Epelle and Gerogiorgis, 2018b), on the computed particle

drag. Alternatively, open-source CFD codes like OpenFoam may be utilised for direct modifications.

There is also a growing need for robust control schemes for real-time monitoring and evaluation of hole cleaning efficiencies during drilling operations. This has hardly been studied before. Integrating optimal control schemes with time-consuming CFD simulations is a formidable task that has limited research efforts in this direction. The use of surrogate/reduced-order modelling methodologies to approximate CFD simulations holds considerable potential for real-time optimisation and control of cuttings transport systems. Such methods will aid the rapid removal of cuttings and the generation of relevant information (rock porosity, permeability and other geomechanical properties), required for the optimal planning of other processes like hydraulic fracturing and other relevant production operations.

6. Acknowledgements

The authors gratefully acknowledge the financial support of the University of Edinburgh for the provision of software licenses used in our computations.

7. Declaration of Interest

The authors declare that they have no known competing financial interests or personal relationships that could have appeared to influence the work reported in this paper.

8. Credit Author Statement

- **Emmanuel I. Epelle:** Conceptualization, Methodology, Software, Data Curation, Writing Original Draft
- **Winifred Obande:** Review and Editing, Resources, Visualization
- **Jude A. Okolie:** Review and Editing, Visualization
- **Tabbi Wilberforce:** Review and Editing, Visualization
- **Dimitrios I. Gerogiorgis:** Conceptualization, Review and Editing, Resources, Funding Acquisition

9. Nomenclature

9.1 Latin letters

A,B,c,d	Coefficients of the Syamlal-O'Brien drag model (-)
AV	Axial velocity (m.s^{-1})
c_t	Cuttings concentration threshold

C_D	Drag coefficient (-)
CMC	Carboxymethyl cellulose solution
d_c	Casing diameter (m)
d_{dp}	Drill pipe diameter (m)
e	Eccentricity (-)
EE	Eulerian-Eulerian model (-)
e_{ss}	Coefficient of restitution (-)
F_r,n,p	Constants in the frictional pressure equation
$\vec{F}_{lift,s}$	Lift force (N)
$\vec{F}_s$	External body force (N)
$\vec{F}_{wl,s}$	Wall lubrication force (N)
$\vec{F}_{d,s}$	Turbulent dispersion force (N)
$\vec{F}_{lift,s}$	Lift force (N)
$\vec{F}_{vm,s}$	Virtual mass force (N)
$\vec{F}_{td,s}$	Turbulent dispersion force (N)
g	Gravitational acceleration (m.s^{-2})
$g_{0,ss}$	Compressibility transition function (-)
I_{2D}	Second variant of the deviatoric stress (-)
$\bar{\bar{I}}$	Unit tensor (-)
K_{sl}	Interphase momentum exchange coefficient (-)
K	Consistency index (Pa.s^n)
L	Length (m)
LE	Lagrangian-Eulerian model
$\dot{m}_{sl}$	Mass transfer from phase s to phase l (kg.s^{-1})
$\dot{m}_{ls}$	Mass transfer from phase l to phase s (kg.s^{-1})
n	Flow behaviour index (-)
p	Pressure (Pa)
p_s	Solids pressure (Pa)
Re_s	Particle Reynolds number (-)
RV	Radial velocity (m.s^{-1})
S_q	Source term (-)
TV	Tangential velocity (m.s^{-1})
τ_0	Yield Stress (N.m^{-2})
u_m	Mean flow velocity (m.s^{-1})
$\vec{v}_{sl}$	Interphase velocity (m.s^{-1})
$\vec{v}_s$	Solid-phase velocity (m.s^{-1})
$\vec{v}_l$	Liquid phase velocity (m.s^{-1})
$v_{r,s}$	Terminal velocity (m.s^{-1})
VF	Volume fraction (-)
VM	Velocity magnitude (m.s^{-1})

9.2 Greek letters

a_s	Solid phase volume fraction (-)
$a_{s,max}$	Solid volume fraction at maximum packing (-)

$a_{s,min}$ Solid volume fraction after which friction occurs (-)
a_l Liquid phase volume fraction (-)
$\mu_{s,\,kin}$ Kinetic viscosity (Pa.s)
$\mu_{s,\,fr}$ Frictional viscosity (Pa.s)
λ_s Bulk viscosity (Pa.s)
λ_q Primary phase bulk viscosity (Pa.s)
μ_l Fluid viscosity (Pa.s)
μ_q Primary phase viscosity (Pa.s)
Θ_s Granular temperature (K)
ϱ_s Solid phase density (kg.m^{-3})
$\varrho_{r,s}$ Phase reference density (kg.m^{-3})
ϱ_q Primary phase density (kg.m^{-3})
ϱ_f Fluid density (kg.m^{-3})
$\hat{\rho}_q$ Effective phase density (kg.m^{-3})
β Dimensionless annular distance (-)
ϕ Angle of internal friction (degrees)
ϕ_{ls} Energy exchange between fluid and solid phases (kg.m^{-1}s^{-3}))
a_l Fluid phase volume fraction (-)
a_s Solid phase volume fraction (-)
τ Shear stress (N.m^{-2})
$\bar{\bar{\tau}}_s$ Solid-phase stress tensor (-)
γ Shear rate (s^{-1})
$\gamma_{\Theta s}$ Collisional dissipation of energy (kg.m^{-1}s^{-3})

10. References

Akhshik, S., Behzad, M. and Rajabi, M., 2015. CFD–DEM approach to investigate the effect of drill pipe rotation on cuttings transport behavior. *J. Pet. Sci. Eng.* 127, 229–244.

ANSYS Fluent, 2017. ANSYS Fluent theory guide 17.1. Ansys Inc, U.S.A.

Awad, A.M., Hussein, I.A., Nasser, M.S., Karami, H. and Ahmed, R., 2021. CFD modeling of particle settling in drilling fluids: Impact of fluid rheology and particle characteristics. *J. Pet. Sci. Eng.,* 199, 108326.

Dalla Valle, J.M., 1943. Micromeritics the Technology of Fine Particles. Pitman Publishing Corporation. New York.

Demiralp, Y., 2014. Effects of Drill-Pipe Whirling Motion on Cuttings Transport Performance for Horizontal Drilling. Louisiana State University, USA, Master dissertation.

Dewangan, S.K., 2021. Effect of eccentricity and inner pipe motion on flow instability for flow through annulus. *SN App. Sci.,* 3(4), 1-15.

Duan, M., Miska, S., Yu, M., Takach, N., Ahmed, R. and Hallman, J., 2010. Experimental study and modeling of cuttings transport using foam with drill pipe rotation. *SPE Drill. Completion*, *25*(03), 352–362.

Epelle, E.I. and Gerogiorgis, D.I., 2017. A multiparametric CFD analysis of multiphase annular flows for oil and gas drilling applications. *Comput. Chem. Eng.,* 106, 645–661.

Epelle, E.I. and Gerogiorgis, D.I., 2018a. Transient and steady state analysis of drill cuttings transport phenomena under turbulent conditions. *Chem. Eng. Res. Des.,* 131, 520–544.

Epelle, E.I. and Gerogiorgis, D.I., 2018b. CFD modelling and simulation of drill cuttings transport efficiency in annular bends: effect of particle sphericity. *J. Pet. Sci. Eng.*, *170*, 992–1004.

Epelle, E.I. and Gerogiorgis, D.I., 2019. Drill cuttings transport and deposition in complex annular geometries of deviated oil and gas wells: A multiphase flow analysis of positional variability. *Chem. Eng. Res. Des.*, 151, 214–230.

Epelle, E.I. and Gerogiorgis, D.I., 2020. A review of technological advances and open challenges for oil and gas drilling systems engineering. *AIChE J.*, 66(4), e16842.

Han, S., Hwang, Y., Woo, N., Kim, Y., 2010. Solid–liquid hydrodynamics in a slim hole drilling annulus. *J. Pet. Sci. Eng.* 70 (3), 308–319.

Heydari, O., Sahraei, E., & Skalle, P., 2017. Investigating the impact of drill pipe's rotation and eccentricity on cuttings transport phenomenon in various horizontal annuluses using computational fluid dynamics (CFD). *J. Pet. Sci. Eng.* 156, 801–813.

Huque, M.M., Butt, S., Zendehboudi, S. and Imtiaz, S., 2020. Systematic sensitivity analysis of cuttings transport in drilling operation using computational fluid dynamics approach. *J. Nat. Gas Sci. Eng.*, 81, 103386.

Jiang, Q., Du, X., Zhu, C., Qi, C., Huang, F. and Wang, S., 2021. Investigation on fluid field characteristics and cinders transport laws in the annulus of grooved drill pipe based on two-phase flow model. *J. Nat. Gas Sci. Eng.*, 103972.

Johnson, P. C., & Jackson, R., 1987. Frictional–collisional constitutive relations for granular materials, with application to plane shearing. *J. Fluid Mech.* 176, 67–93.

Karnis, A., Goldsmith, H.L. and Mason, S.G., 1966. The flow of suspensions through tubes: V. Inertial effects. *The Can. J. Chem. Eng.* 44(4), 181–193.

Kinaci, M. F., 2015. Numerical Investigation of Drag Forces on Particle Clouds in non-Newtonian Flow. University of Duisburg-Essen, Germany, Masters Dissertation.

Kim, S.H., Lee, J.H. and Braatz, R.D., 2020. Multi-phase particle-in-cell coupled with population balance equation (MP-PIC-PBE) method for multiscale computational fluid dynamics simulation. *Comput. Chem. Eng.*, *134*, 106686.

Lun, C., Savage, S., & Jeffrey, D., 1984. Kinetic theories for granular flow: inelastic particles in Couette flow and slightly inelastic particles in a general flow field. *J. Fluid Mech.* 140, 223–256.

Movahedi, H. and Jamshidi, S., 2021. Experimental and CFD simulation of slurry flow in the annular flow path using two-fluid model. *J. Pet. Sci. Eng.*, 198, 108224.

Naganawa, S., Suzuki, M., Ikeda, K., Inada, N. and Sato, R., 2021. Modeling Cuttings Lag Distribution in Directional Drilling to Evaluate Depth Resolution of Mud Logging. *SPE Drill. Completion*, 36(01), 63–74.

Pang, B., Wang, S., Liu, G., Jiang, X., Lu, H. and Li, Z., 2018. Numerical prediction of flow behavior of cuttings carried by Herschel-Bulkley fluids in horizontal well using kinetic theory of granular flow. *Powder Technol.*, 329, 386-398.

Qi, D. and Luo, L.S., 2003. Rotational and orientational behaviour of three-dimensional spheroidal particles in Couette flows. *J. Fluid Mech.* 477, 201–213.

Rasool, M.H., Zamir, A., Elraies, K.A., Ahmad, M., Ayoub, M. and Abbas, M.A., 2021. Investigative Review on Cutting Transportation Ability of Ionic Liquid-Based Drilling Mud. *J. Hunan University Nat. Sci. 48*(2).

Rooki, R., Ardejani, F.D., Moradzadeh, A. and Norouzi, M., 2015. CFD Simulation of Rheological Model Effect on Cuttings Transport. *J. Dispersion Sci. Technol.* 36(3), 402–410.

Schaeffer, D., 1987. Instability in the evolution equations describing incompressible granular flow. *J. Diff. Eqns.* 66(1), 19–50.

Siddhamshetty, P., Mao, S., Wu, K. and Kwon, J.S.I., 2020. Multi-size proppant pumping schedule of hydraulic fracturing: Application to a MP-PIC model of unconventional reservoir for enhanced gas production. *Processes*, *8*(5), 570.

Sorgun, M., 2010. Modeling of Newtonian Fluids and Cuttings Transport Analysis in High Inclination Wellbores with Pipe Rotation. Middle East Technical University, Turkey, Doctoral dissertation.

Syamlal, M. and O'Brien, T.J., 1987. The derivation of a drag coefficient formula from velocity-voidage correlations. Technical Note, US Department of Energy, Office of Fossil Energy, NETL, Morgantown, WV.

Subramaniam, S., 2013. Lagrangian–Eulerian methods for multiphase flows. *Prog. Energy Combust. Sci.*, 39 (2), 215–245.

Syamlal, M., Rogers, W. and O'Brien, T.J., 1993. MFIX documentation: Theory guide. National Energy Technology Laboratory, Department of Energy, Technical Note DOE/METC-95/1013 and NTIS/DE95000031.

Verma, V. and Padding, J.T., 2020. A novel approach to MP-PIC: Continuum particle model for dense particle flows in fluidized beds. *Chem. Eng. Sci.: X*, *6*, 100053.

Wan, Z., Yang, S. and Wang, H., 2021. MP-PIC investigation of the multi-scale gas-solid flow in the bubbling fluidized bed. *Exp. Comput. Multiphase Flow*, *3*(4), 289-302.

Wang, S., Wang, Y., Wang, R., Yuan, Z., Chen, Y., Shao, B. and Ma, Y., 2021. Simulation study on cutting transport in a horizontal well with hydraulic pulsed jet technology. *J. Pet. Sci. Eng.*, 196, 107745.

Yan, T., Qu, J., Sun, X., Chen, Y., Hu, Q., Li, W. and Zhang, H., 2020. Numerical investigation on horizontal wellbore hole cleaning with a four-lobed drill pipe using CFD-DEM method. *Powder Technol.*, 375, 249–261.

Yilmaz, D., 2012. Discrete Phase Simulations of Drilled Cuttings Transport Process in Highly Deviated Wells. Louisiana State University, USA, Master dissertation.

Zaisha, M., Chao, Y., Kelessidis, V., 2012. Modeling and numerical simulation of yield viscoplastic fluid flow in concentric and eccentric annuli. *Chin. J. Chem. Eng.* 20(1), 191–202.

Zhu, X., Shen, K., Li, B. and Lv, Y., 2019. Cuttings transport using pulsed drilling fluid in the horizontal section of the slim-hole: An experimental and numerical simulation study. *Energies*, 12(20), 3939.

Zhu, Z., Song, X., Li, G., Xu, Z., Zhu, S., Yao, X. and Jing, S., 2021. Prediction of the settling velocity of the rod-shaped proppant in vertical fracture using artificial neural network. *J. Pet. Sci. Eng.*, 200, 108158.